Available online at www.sciencedirect.com

ScienceDirect

Procedia Engineering 130 (2015) 973 – 985

Procedia Engineering

www.elsevier.com/locate/procedia

14th International Conference on Pressure Vessel Technology

# Characterising Residual Stresses in a Dissimilar Metal Electron Beam Welded Plate

K. Abburi Venkata[a,]*, C.E. Truman[a], D.J. Smith[a]

[a]*University of Bristol, Solid Mechanics Research Group, Department of Mechanical Engineering, Bristol, BS81TR, UK*

**Abstract**

Dissimilar metal welded components are becoming increasingly common in industrial applications especially in the nuclear sector. Dissimilar metal welding refers to the joining of two materials from different alloy groups. One of the basic requirements of the dissimilar metal welded joint is that the joint strength should be greater than or equal to that of the weakest member and a careful characterisation of the joint is crucial before considering the applicability of the dissimilar metal welded components. The current paper explores the feasibility of an electron beam welded joint between ferritic/martensitic Grade 91 or more commonly known as modified P91 and austenitic 316LN stainless steel, without the addition of any filler material. The residual stress distribution arising from the welding is determined from measurements using neutron diffraction experiment and predictions using finite element analysis. The measured data has been analysed using Rietveld and single peak fits. The finite element analysis was conducted on a two-dimensional cross-sectional model using ABAQUS code, implementing the effects of solid-state phase transformation experienced by P91 steel. The predicted residual stresses are compared with the experimental measurements and conclusions are drawn on the final residual stress distribution.



Peer-review under responsibility of the organizing committee of ICPVT-14

*Keywords:* Dissimilar metal welding; electron beam welding; neutron diffraction; finite element modelling; residual stresses.

## 1. Introduction

The Prototype Fast Breeder Reactor (PFBR) is a 500 MWe sodium-cooled fast breeder nuclear reactor presently being constructed in Kalpakkam, India [1]. The Indira Gandhi Centre for Atomic Research (IGCAR) is responsible

* Corresponding author.
*E-mail address:* k.abburivenkata@bristol.ac.uk



Peer-review under responsibility of the organizing committee of ICPVT-14
doi:10.1016/j.proeng.2015.12.250

for the design of this reactor. The cooling system of the reactor uses liquid sodium and requires additional safety measures to isolate the coolant from environment. The steam generator, made of modified 91 steel, is connected to the intermediate heat exchanger, made of AISI 316LN stainless steel with a dissimilar metal weld. The schematic of the rector system is shown in Fig 1(a) and the steam generator with the dissimilar metal weld in Fig 1(b). Currently the dissimilar metal weld is a tri-metallic transition joint and uses a multi-pass Tungsten Inert Gas (TIG) welding. The complex design of the joint was necessary to minimise thermal stresses. The arrangement of the welded joint is shown in Fig 2(a) [2]. ER16-8-2 is a filler material with 16% Cr 8% Ni and 2% Mo, used for high temperature austenitic stainless steels. Alloy 800 is an Inconel alloy with very good creep rupture properties above 600 °C. Inconel 182 is an electrode used in dissimilar metal welds of stainless steels joined to carbon steels.

Experience with dissimilar metal weld joints has shown that a considerable number of failures occurred at a very early stage in service than expected, especially in power plants [3]. An extensive failure analysis was carried out at IGCAR on dissimilar metal welds between 2.25Cr-1Mo ferritic steel and AISI type 316 stainless steel with and without Inconel-82 buttering using the non-destructive X-ray diffraction (XRD) technique and to assess the effectiveness of the buttering on the extent of reduction in the residual stress [4]. Various earlier studies that characterise residual stresses in dissimilar metal welds using conventional welding process are available in the literature [3, 5–9].

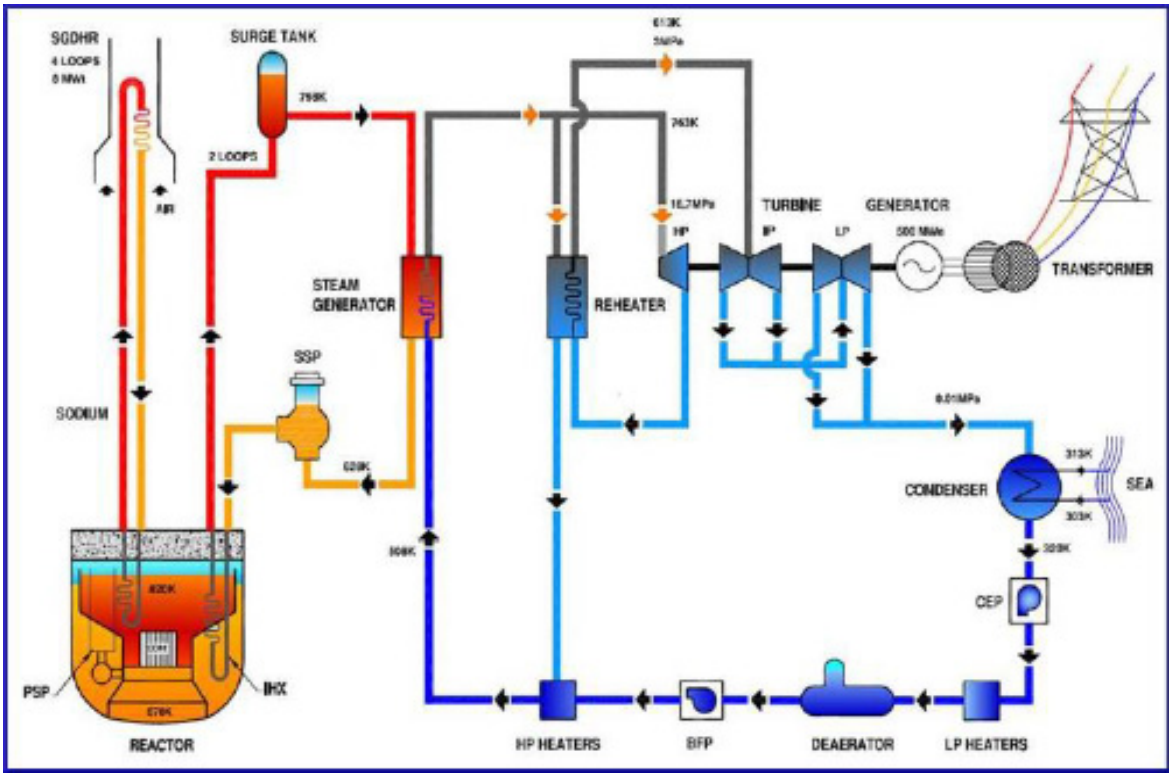


(a) Schematic of the prototype fast breeder reactor

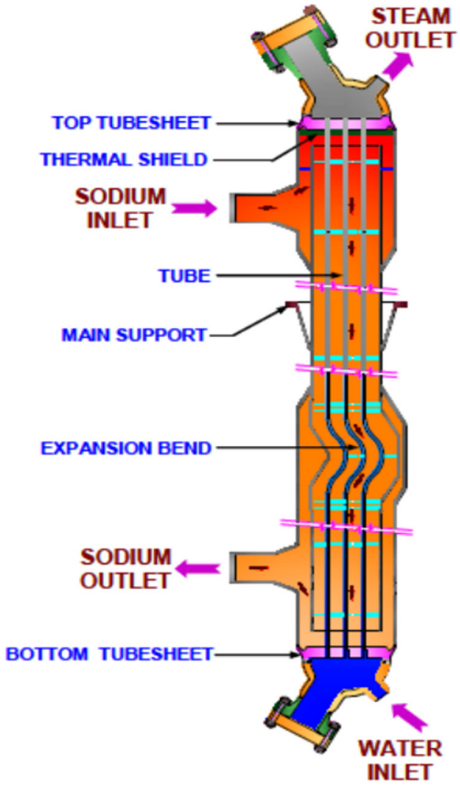


(b) Schematic of the steam generator and the dissimilar metal weld

Fig. 1. Typical heat transport system in fast breeder reactor [1].


(a) Trimetallic joint with filler material

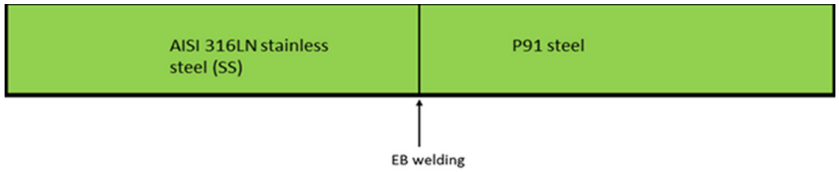


(b) EB welded joint without any filler material

Fig. 2. Schematic of the existing trimetallic joint and the proposed EB joint [1].

To avoid the complex design, it is proposed that the two dissimilar metals, ferritic/martensitic P91 steel and AISI 316LN austenitic steel are joined using EB welding. This is shown in Fig 2(b) [2]. An overview of the application of

EB welding to dissimilar metals is provided by Sun and Karppi [10]. In this research, the welded joints were characterised using neutron diffraction experiment and finite element analysis. One of the primary interests of the experiment was to obtain the variation of the residual stresses through the thickness of the plate at the centre of the weld, to determine the magnitude of the inter-phase stresses and understand the influence of these on the joint performance. These stresses can play an important role in localised failure arising from microstructural variations. Another important aspect is to establish the significance of martensitic phase transformation related volume change experienced by the P91 steel, during cooling of the weld, on the final residual stress distribution. It is essential to understand the contribution of this volume change towards the interphase stress state and thereby the macro stress state observed in the joint.

## 2. Sample details

The sample was a dissimilar metal joint made from modified 9Cr-1Mo (P91), a ferritic/martensitic steel joined to AISI 316LN austenitic stainless steel, using electron beam welding. The dimensions of the welded plate were 250mm x 155mm x 11 mm. The width of the fusion zone was ~ 1.4mm and that of the HAZ was ~ 1 mm. The arrangement of the plate during welding is shown in Fig 3(a). The outer edges of the plates were clamped to larger steel plates to restrain the sample plates during welding. The cross-sectional weld macrograph is shown in Fig 3(b). The chemical composition of the materials is shown in Table 1. The welding process was autogenous, without the addition of any filler material. A beam current of 48mA and a gun voltage of 120 kV were used for the full penetration welding. The speed of the welding gun was 500mm/min. In order to facilitate the welding process and retain the weld plates in position, as shown in Fig 3(a), tack welds were laid along the weld seam in the direction of welding using EB welding and through the thickness of the plate at the start end of the weld using TIG welding. Also the joining edges were melted up to a depth of 1.5mm prior to full penetration welding, to hold the plates in place. Preheating was done on the modified P91 steel side to compensate for the differential thermal conductivities of both the metals. AISI 316LN stainless steel has a lower thermal conductivity than that of modified P91 steel, which could lead to heat accumulation and higher amount of melting in 316LN stainless steel. After the welding pass, an additional cosmetic/smoothing pass was introduced using a defocussed beam with 26mA and 100 kV which resulted in a penetration depth of 4.5 mm. The purpose of the smoothing pass was to enhance the surface finish and to minimise any post weld machining processes.

## 3. Experimental set-up

Neutron diffraction measurements were conducted on the ENGIN-X instrument at the ISIS facility, Rutherford Appleton Laboratory, on the dissimilar metal joint to obtain residual strains and thereby stresses. Pulsed sources such as the one at ISIS, produces diffraction pattern over a range of grain families oriented along various crystallographic planes and permitted the residual stress/strain state at a micro level between the two phases to be measured [14, 15]. The plates were measured in the as-welded condition. Measurements were made along two different lines, (i) across the weld at the centre of the plate, at a depth of 5.5mm from the top surface and (ii) through the thickness of the plate at the weld centre. Owing to the very narrow dimensions of the fusion zone and heat affected zone (HAZ) in the sample, a small gauge volume of 1mm x 1mm x 1mm was used to capture the steep gradients of stress, for the measurements of lattice constant along the weld (longitudinal). However, based on the assumption that there was limited variation in the longitudinal strain along the weld seam, the gauge volume was extended to 10mm while making measurements in transverse and normal directions. This reduced the overall measurement time for each measurement point. For measurements on reference samples described later, the gauge volume was maintained as 1mm x 1mm x 1mm in all orientation

As the cosmetic pass had a penetration depth of 4.5 mm, it was decided to measure the stresses from the initial pass alone at a depth of 5.5mm from the top surface. The measurement points in the weld and the HAZ region were evenly spaced at distances of 0.5mm on either side of the weld fusion line. Outside the HAZ/Parent boundary of the weld the points were almost 2mm to 15mm apart on either side of the fusion line. For through thickness measurements, the points were selected at depth increments of 1.5mm from the top surface. In order to measure the lattice spacing in a stress-free state, two different $d_0$ samples were machined from the welded plate. A 2mm thick

slice was machined from an end of the plate along the transverse edge. This slice was then machined to create $d_0$ samples as shown in Fig. 4. Two matchstick samples were extracted from the ends of the slice on both sides to act as reference samples for the base metals. A comb sample was extracted from the centre of the slice with regions from weld fusion zone and the HAZ on either side of the fusion zone acting as a reference sample.

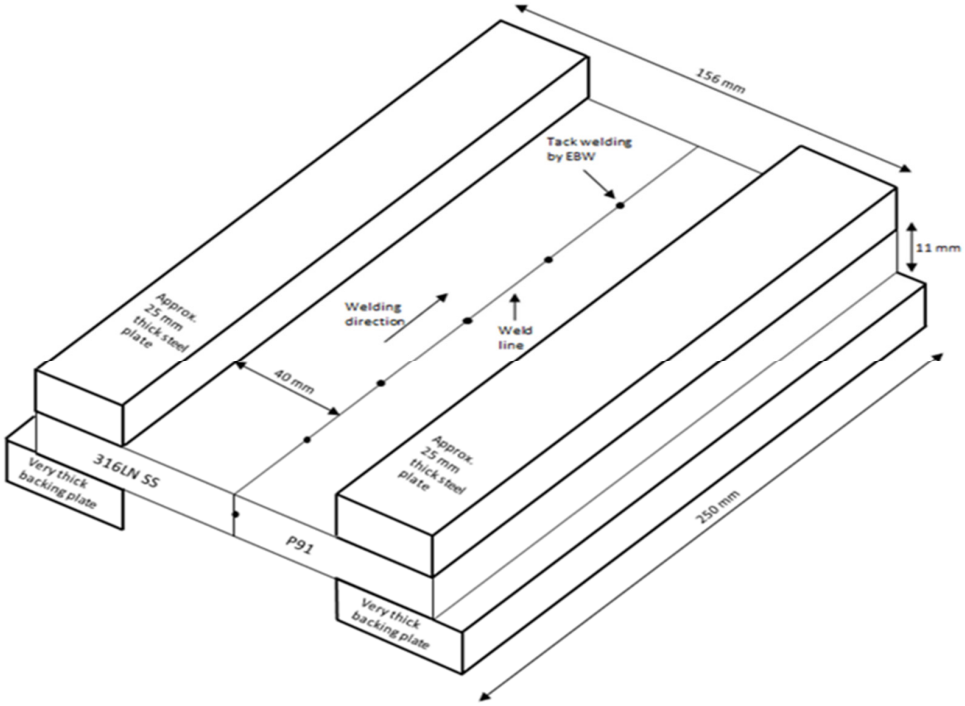


(a) Schematic of the dissimilar metal EB welded sample with restraining larger steel plates

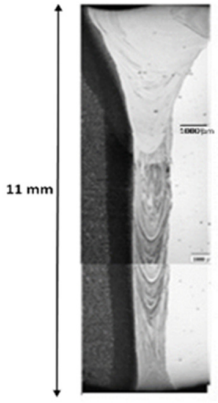


(b) Cross-sectional weld macrograph

Fig. 3. Dissimilar metal EB welded sample

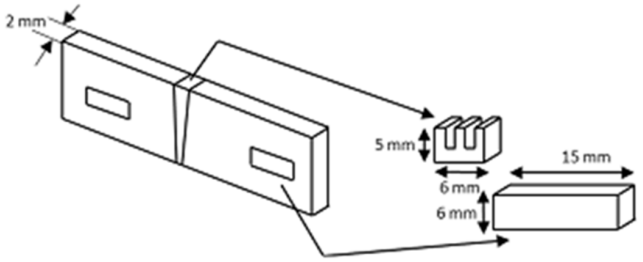


Fig. 4. Schematic of the $d_0$ specimens.

Table 1. Chemical composition of the base metals in % wt. (Balance Fe) [11 – 13].

| | C | Mn | Zr | Si | P | S | Cr | Mo | Ni | Cu | Al | N | Nb | Ti | V | |
|---|---|---|---|---|---|---|---|---|---|---|---|---|---|---|---|---|
| P91 | 0.11 | 0.39 | 0.005 | 0.27 | 0.017 | 0.003 | 8.82 | 0.82 | 0.21 | 0.17 | 0.02 | 0.0464 | 0.07 | 0.004 | 0.2 | |
| 316 LN | 0.03 | 1.72 | - | 0.39 | 0.025 | 0.003 | 17.5 | 2.58 | 11.9 | 0.195 | 0.001 | 0.087 | 0.005 | 0.005 | 0.051 | |

Based on the sample geometry and the planes of symmetry, the principal directions were assumed to coincide with the residual stress directions in the three orthogonal directions. Measurements were made in the three principal stress directions, corresponding to longitudinal, transverse and normal directions of the weld, on the stressed as well as the stress-free reference samples. As the neutrons were from a pulsed source, the reflections were obtained from different families of grains and Pawley-Rietveld refinement was used to fit the diffraction peaks. Direction and position dependent lattice spacings on the stress-free samples were used to calculate the strains in the respective stress directions. The strains were calculated using [14, 15],

$$\varepsilon_{xx} = \frac{a_x - a_{0x}}{a_{0x}} \tag{1}$$

where $\varepsilon_{xx}$ is the strain along the direction $x$, $a_x$, $a_{0x}$ are the lattice constant measured in the stressed and stress-free sample in the direction $x$. The stresses were calculated using [14, 15],

$$\sigma_{ij} = \frac{E}{(1+\nu)}\left[\varepsilon_{xx} + \frac{\nu}{(1-2\nu)}\left(\varepsilon_{xx} + \varepsilon_{yy} + \varepsilon_{zz}\right)\right] \tag{2}$$

where $E$ is the Young's modulus and $\nu$ is the Poisson's ratio. The value of Young's modulus was assumed to be 210 GPa for P91 steel and 195.6 GPa for AISI 316LN stainless steel respectively. These values correspond to the recommendations from Kroner's models for the macroscopic elastic bulk properties in ploy-crystals for the bcc and fcc phases respectively [15].

## 4. Electron beam weld simulations

A numerical analysis was conducted on the 2D cross-sectional plane at mid-thickness to simulate the electron beam welding of the dissimilar metal plates and predict the residual stresses and strains using ABAQUS finite element code. As the welding speed was high, the centre of the plate was assumed to be at a steady-state condition, unaffected by the transient effects of welding, therefore it was assumed that a 2D model of the cross-section at the centre of the plate predicted the thermal history and weld residual stresses with sufficient accuracy [16–19]. The welding simulation was carried out in 2 stages using sequentially coupled thermal and mechanical analyses. First

order linear quadratic and triangular heat transfer elements (DC2D4 & DC2D3) were used in the thermal analysis whereas linear plane strain elements with reduced integration and triangular elements (CPE4R&CPE3) were used in the mechanical analysis. Temperature dependent material properties and stress-strain data were used in the analysis for both the materials. The finite element mesh used in the analysis is shown in Fig 5. The temperature dependent thermo-physical properties and the monotonic stress-strain values of the austenitic 316LN stainless steel and that of P91 steel are described elsewhere [20].

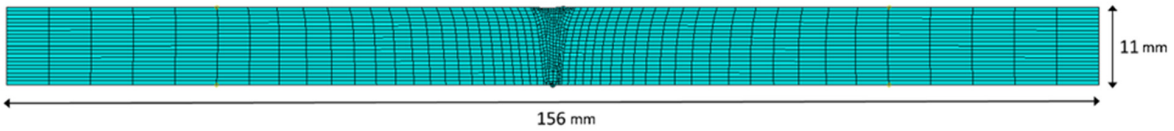


Fig. 5. Finite element mesh of the 2D cross-sectional model for dissimilar metal EB welded plate [20].

Both the welding pass and the cosmetic pass were modelled in the analysis. Spot welds made at the beginning of the welding process were neglected in the analysis. The thermal analysis was conducted using block dumped approach [18, 19, 21]. The volumetric heat flux applied to the weld elements were calculated from the welding parameters, weld pool size and the mesh dimensions. The weld efficiency was assumed to be 90%. The heat flux corresponding to the full penetration weld pass was applied during the heating step. After welding, the plate was cooled to 20 °C. Then the weld elements were subjected to another volumetric heat flux corresponding to the cosmetic pass resulting in a depth of penetration of ~ 4.5 mm. The plate was subsequently cooled to 20 °C. The heat loss from the plate was simulated using radiation boundary condition only with an emissivity of 0.75. The preheating on the P91 steel side before actual welding was not considered in the analysis. Also it was assumed in the analysis, that the conduction between the specimen and the backing plate had no significance in the thermal solution and was therefore neglected.

P91 steel undergoes solid-state phase transformation during the cooling cycle. This was modelled in the analysis for the portion of the plate that corresponds to the P91 side. The phase transformation was implemented using a user-subroutine UEXPAN. The thermal expansion coefficient of P91 steel between the martensite start temperature (~ 400 °C) and martensite finish temperature (~ 200 °C) was changed to account for the change in the volume during the transformation. The total volume change associated with the transformation was considered as 0.0025mm/mm [13]. The martensitic fraction was calculated from Koistinen-Marburger relationship explained elsewhere [17, 22, 23]. The volume change arising from austenitic transformation and transformation plasticity during phase transformation were neglected. The mechanical analysis was conducted after the thermal analysis and the residual stresses and strains were predicted. The material hardening behaviour was assumed to be isotropic for both the materials with single stage annealing at 850 °C for P91 steel and 1050 °C for 316LN stainless steel. Mechanical boundary conditions were applied to simulate the clamping conditions on the plate as well as to prevent the rigid body motion.

## 5. Results and Discussion

### *5.1. Neutron diffraction results*

The neutron diffraction experiment resulted in the determination of the lattice spacing, and subsequently stresses and strains were calculated. The results are presented and discussed in this section. The stress-free lattice spacings in the reference samples are shown in Fig 6 for both fcc and bcc phases. There was a variation in the lattice spacing from the fusion, HAZ and parent regions in the welded sample. The strain profiles across the weld are shown in Fig 7. It can be seen that at the weld centre the results indicate the presence of both tensile and compressive strains, which is not possible at a macro-stress level. This indicated that the diffraction pattern at the centre of the profile had both fcc and bcc phases, suggesting a local segregation between fcc and bcc phases in the fusion zone. The

diffraction pattern was representative of the inter-phase strains [24, 25]. Since a narrow gauge volume was used for the measurements, the sampling volume was not large enough for the inter-phase stresses to be equilibrated. Therefore the phase dependent strains were obtained rather than the macro strains.

The strain profiles through the thickness of the weld are shown in Fig 8 and the phase dependency of the strains is illustrated. The fcc phase was predominantly under tension, whereas the bcc was under compression. This was a consequence of martensitic phase transformation related volume change during rapid cooling. During rapid cooling, P91 steel experiences a thermal dilation upon reaching the martensitic start temperature, until the martensitic finish temperature, resulting in compressive strains in the weld regions and high tensile strains adjacent to the HAZ/Parent boundary. Therefore the weld fusion region had compressive strains in the bcc phase and tensile strains in fcc phase [25].

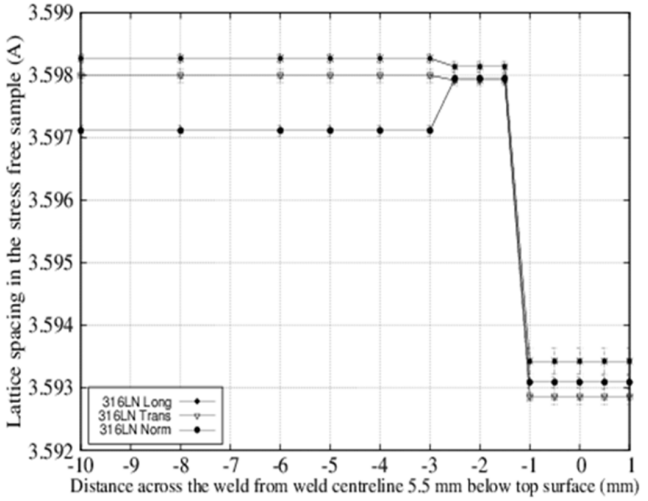


(a)

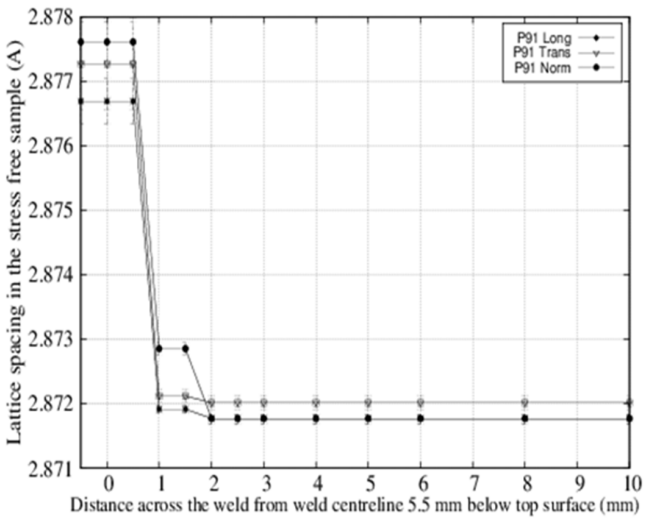


(b)

Fig. 6. Stress-free lattice spacing in (a) fcc phase (b) bcc phase.

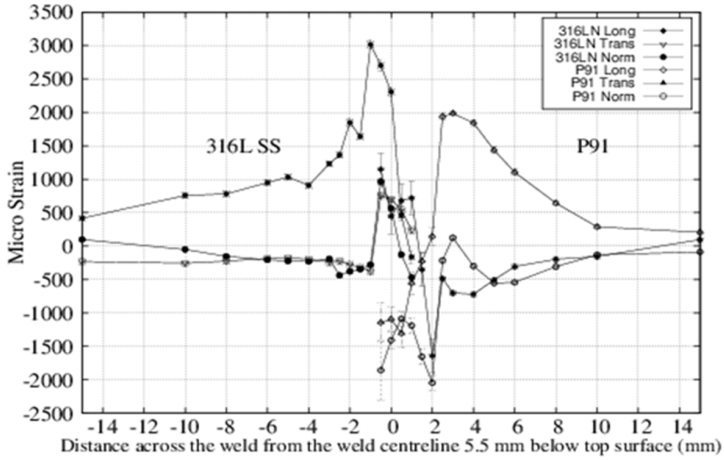


Fig. 7. Strain across the weld in 316LN and P91 materials.

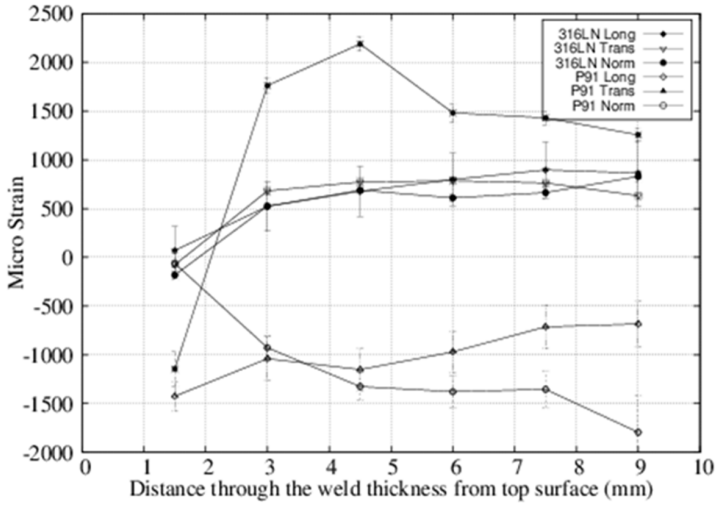


Fig. 8. Strain through the weld fusion zone at the weld centre.

The residual stress profiles determined using eq. (2) across the weld and through the thickness of the plate are shown in Fig 9 and 10 respectively. The peak tensile stress in the longitudinal direction was 800 MPa in the HAZ region on the AISI 316LN stainless steel side. Such a high magnitude of stress may have resulted from partial filling of the sampling gauge volume creating pseudo strains. As the $d_0$ samples were small, there might be only partial filling of the gauge volume, resulting in a corresponding peak broadening, often misinterpreted as strain. Also, the $d_0$ specimens were extracted from regions under the influence of the cosmetic pass, whereas the measurements on the specimen are made in a region away from the influence of the cosmetic pass. This suggests that the microstructure of the $d_0$ specimens and their lattice spacing could be considerably different from that of the weld specimen.

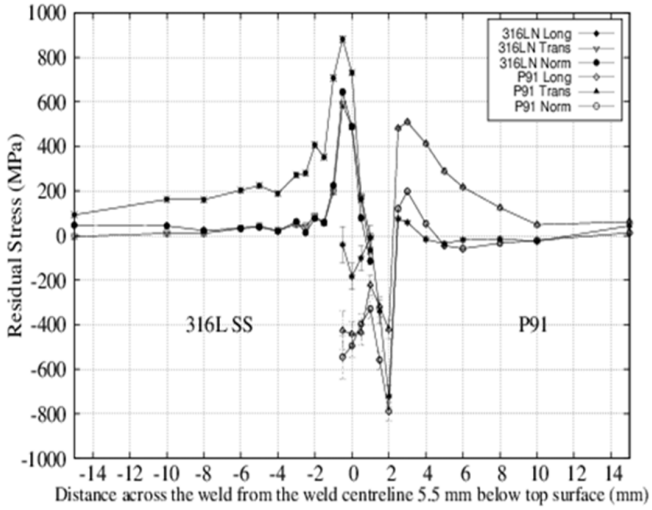


Fig. 9. Stress across the weld in 316LN and P91 materials.

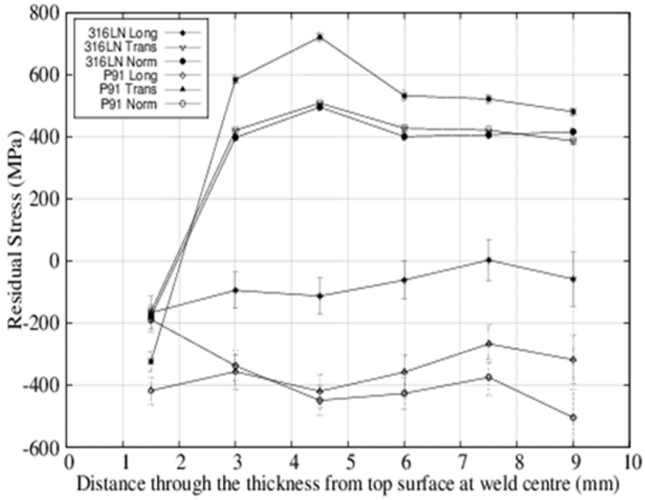


Fig. 10. Stress through the weld fusion zone at the weld centre.

### *5.2. Finite element results*

A contour map showing the longitudinal residual stress across the weld at mid cross-section is shown in Fig 11. From the contour, the stresses at the interface of the weld joint, where both the phases are present, are ambiguous showing both tensile and compressive stresses. It can be reasoned that the stress state is representative of the inter-phase stresses rather than the macro stresses. A comparison of the predicted and measured longitudinal stress, across the weld at the depth of 5.5 mm from the top surface, is shown in Fig 12. The predicted residual stresses through the thickness of the plate at the weld centre for the bcc and the fcc phases are captured in Fig 13, with those from the experiment. It is observed that the stress state in the fcc phase is tensile whereas in the bcc phase is compressive, resulting from the volume change associated with the phase transformation. This shows that the predictions are

really inter-phase stresses rather than macro-stresses [25]. This is in correlation with the results from the neutron diffraction experiment.

The comparison across the weld agrees very well in the regions outside the weld fusion and HAZ regions. However in the weld fusion and HAZ regions there are significant differences. This can be partly attributed to the absence of representative material data for these regions. Comparison of the stresses through the thickness agrees very well in the regions outside the influence of the cosmetic pass. From the experimental and simulation results, it is evident that a greater understanding of the inter-phase stresses is required to arrive at the macro-stress state.

## 6. Concluding remarks

Based on the neutron diffraction experiment and a finite element analysis for dissimilar metal welded P91 and austenitic 316LN stainless steel plates using EB welding, it was shown that;

1) Dissimilar metal welded samples have fcc and bcc phases present in the weld fusion zone. The narrowness of the fusion zone and the HAZ regions, along with the coarse grains in the weld fusion zone introduced considerable difficulty in obtaining statistically significant counting statistics during the neutron diffraction experiment.
2) The narrow fusion zone and HAZ regions meant that narrow gauge volumes were used and therefore inter-phase residual stresses or type II stresses might not be averaged. In essence the measurements usually reveal the stress state between the phases rather than the macro-stress state. The magnitudes of these phase dependent stresses were created by the volume change arising from the phase transformation in P91 steel.
3) Irrespective of the range of assumptions made in the FE simulations, there was some agreement between measured and simulated residual stresses especially in the regions away from weld fusion zone and HAZ.

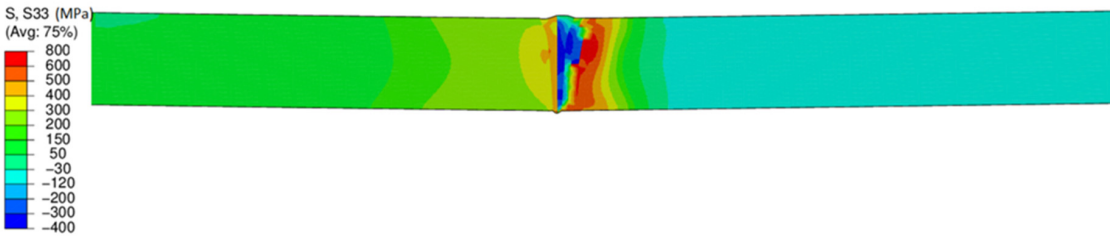


Fig. 11. Contour map showing the longitudinal residual stress profile at mid-section of the plate.

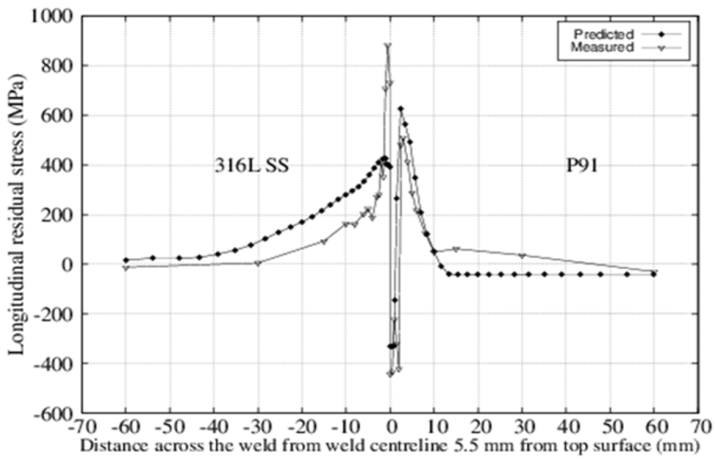


Fig. 12. Comparison of predicted and measured longitudinal residual stress across the weld.

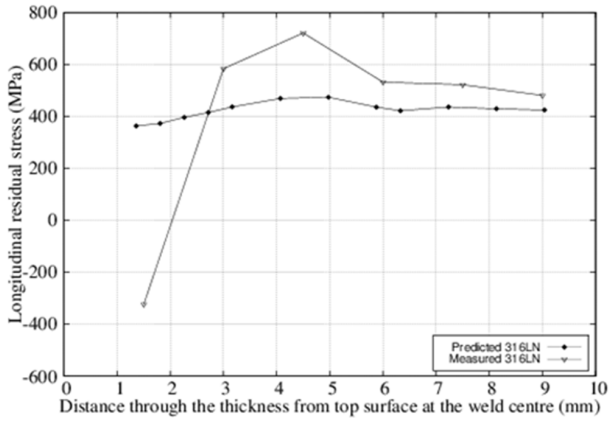


(a)

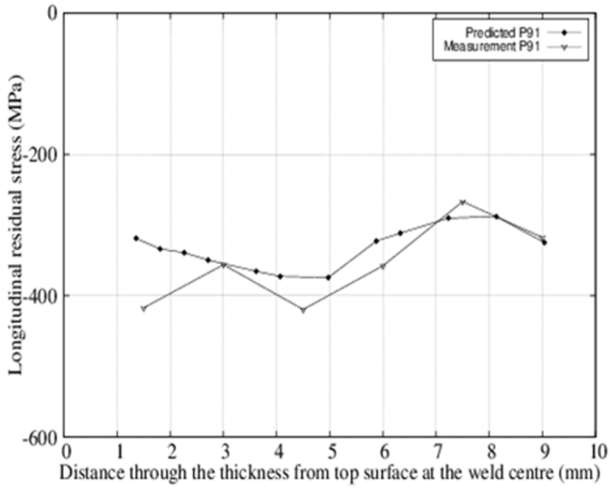


(b)

Fig. 13. Comparison of predicted and measured longitudinal stress through the weld fusion zone at the weld centre (a) fcc phase (b) bcc phase.

## Acknowledgements

We would like to acknowledge the support provided by IGCAR for the samples and ISIS at Oxford, for the valuable advice and support to the residual stress measurements. This project was funded by an EPSRC project EP/K007/866/1.

## References

[1] P. Puthiyavinayagam, S. Raghupathy, A. Balasubramaniyan, P. Selvaraj, P. Mohanakrishnan, S.C. Chetal, P. Chellapandi and Baldev Raj, Current status of fast reactors and future plans in India, Energy Procedia, 2010.

[2] Baldev Raj, S.B. Bhoje, S.L. Mannan and S.C. Chetal, Selection of materials for prototype fast breeder reactor, Techinical report, Indira Gandhi Centre for Atomic Research, Kalpakkam, India, 2004.

[3] T. Jayakumar, A. Joseph, S.K. Rai and N. Murugan, Evolution of residual stresses in dissimilar metal weld joints. International Journal of Pressure Vessels and Piping, 82 (2005), 700 – 705.

[4] T. Jayakumar, A. Joseph, A.S. Ramesh and N. Murugan, Failure analysis of a dissimilar weld joint in a steam generator, Practical Metallurgy, 38 (2001), 667 – 679.
[5] H. Cerjak, The role of welding in the power generation industry, 61st IIW Annual Assembly, 2008.
[6] H. Swenson, M.A. Buechler, M. Steinzing, B. Clausen, M. Kerr, M.B. Prime and T. Sisneros, Residual stress characterisation in a dissimilar metal weld nuclear reaction piping system mock up. Journal of Pressure Vessel Technology, 135 (2013).
[7] L-W.T.W-C. Chung, J-Y. Huang and C. Chen, Microstructure and stress corrosion cracking behaviour of the weld metal in alloy 52-a5208 dissimilar welds, Materials Transactions, The Japan Institute of Metals, 52 (2011), 12 – 19.
[8] V.R.P. Gilles and M. Fontaine, Welding residual stress effect on dissimilar metal weld junction fracture, Proceedings of the 12th International Pressure Vessel Technology, 2009.
[9] C. Faidy, Structural integrity of bi-metallic welds in piping – fracture testing and analysis, Proceedings of Pressure Vessel and Piping, 2008.
[10] Z. Sun and R. Karppi, The application of electron beam welding for the joining of dissimilar metals: an overview. Journal of Materials Processing Technology, 59 (1996), 257 – 267.
[11] P.J. Bouchard, The net bead-on-plate benchmark for weld residual stress simulaiton. International Journal of Pressure Vessels and Piping, 86 (2009), 31 – 42.
[12] A. Kumdu, S. Kumar, K.A. Venkata, J.A. Francis, A. Paradowska, G.K. Dey, P.J. Bouchard and C.E. Truman, Residual stresses in P91 steel electron beam welds, Science and Technology of Welding and Joining, 18 (2013), 70 – 75.
[13] S. Kumar, A. Kundu, K.A. Venkata, A. Evans, J.A. Francis, K. Bhanumurthy, P.J. Bouchard, C.E. Truman and G.K. Dey, Residual stresses in laser welded ASTM A387 Grade 91 steel plates, Materials Science & Engineering A, 575 (2013), 160 – 168.
[14] M.E. Fitzpatrick and A. Lodini, Analysis of residual stress by diffraction using neutron and synchrotron radiation, Taylor and Francis Group, 2003.
[15] T.M. Holden, M.T. Hutchings, P.J. Withers and T. Lorentzen, Introduction to the characterisation of residual stress by neutron diffraction, CRC Press, 2005.
[16] K. Abburi Venkata, C.E. Truman, D.J. Smith, S. Kumar, H.C. Dey and P.J. Bouchard, Study on the effect of post weld heat treatment parameters on the relaxation of welding residual stresses in electron beam welded P91 steel plates, Procedia Engineering, 86 (2014), 223 – 233.
[17] K. Abburi Venkata, C.E. Truman, Finite element simulation of laser welding in a P91 steel plate, Proceedings of the ASME 2013 Pressure Vessels and Piping conference, 2013.
[18] P. Kapadia, K. Abburi Venkata, C. Aird, M.C. Smith and O. Muransky, Round robin predictions of residual stresses in the edge-welded beam R6 valdiation benchmark problem, Proceedings of the ASME 2013 Pressure Vessels and Piping Division Conference, 2013.
[19] A. Tiziani, P. Ferro, H. Porzner and F. Bonollo, The influence of phase transformations on residual stresses induced by the welding process – 3D and 2D numerical models, Materials Science Engineering, 14 (2006).
[20] K. Abburi Venkata, Characterising high energy beam welding in structural steels with numerical simulation and validation, PhD thesis, University of Bristol, 2015.
[21] P.J. Bouchard, Residual stress simulation heat input models for stainless steel manual metal arc welds, Technical report, British Energy, 2003.
[22] D. Dean and M. Hidekazu, Prediction of welding residual stress in multi-pass butt-welded modified 9Cr-1Mo steel pipe incorporating solid state phase transformation, Computational Materials Science, 37 (2006), 209 – 219.
[23] T.H. Hyde, A.A. Becker, A.H. Yaghi and W. Sun, Finite element simulation of welding and residual stresses in a P91 steel pipe incorporating solid state phase transformation and post-weld heat treatment, Journal of Strain Analysis, 43 (2008), 275 – 293.
[24] M.R. Raymond, E.C. Oliver and P.J. Withers, Interphase and intergranular stress generation in carbon steels, Acta Materialia, 52 (2004), 1937 – 1951.
[25] S. Torii, S. Harjo, Y. Tomato and T. Kamiyama, Residual thermal phases stresses in $\alpha - \gamma$ Fe – Cr – Ni alloys measured by a neutron diffraction time-of-flight method, Materials Transactions, The Japan Institute of Metals, 43 (2002), 1696 – 1702.